Progress In Electromagnetics Research C, Vol. 119, 17–30, 2022

Compact Negative-Permittivity Microstrip Patch Antenna for End-Fire Radiation

Masoud Ahmadi[1, *], Bruce Veidt[2], and Loïc Markley[1]

Abstract—We propose a compact microstrip patch antenna that uses a negative permittivity substrate to achieve an end-fire radiation pattern. The antenna is designed to operate at X-band frequencies with a patch footprint of $0.9\lambda \times 0.05\lambda$ and a thickness of $\lambda/20$. We show that loading a narrow patch with a negative permittivity substrate introduces an effective shunt inductance that resonates with the strong fringing capacitance of the patch. At resonance, the electric field is vertically polarized and approximately uniform across the patch, producing transverse nulls that improve the directivity of the antenna. The negative permittivity substrate is implemented using a thin-wire effective medium with four vias spread across the patch. The antenna is matched to $50\,\Omega$ using a quarter-wavelength transformer. The fabricated antenna operates at 10.8 GHz with a peak return loss of 30 dB and a bi-directional directivity of 10.7 dBi. The antenna has a 10-dB impedance bandwidth of 3.8% and radiates with a simulated efficiency of 93%.

1. INTRODUCTION

As modern-day wireless communication devices become increasingly small and light, the demand for compact planar antenna designs is high. In low-path-loss communication channels, such as mines, bridges, tunnels, roadways, and city corridors, a bi-directional radiation pattern can provide higher signal strengths and improved data rates [1–7]. Bi-directional patterns are typically achieved using antenna arrays, which can provide high gains but require larger footprints [8–14]. Many of these antennas are particularly well-suited for the use in low path-loss environments because they are also designed to radiate parallel to the reflective surface of a large conducting body, such as a vehicle, a road, or a tunnel side wall [15–17].

The development of microstrip technology has introduced a range of low-cost and easily-integrable antennas in a low-profile, conductor-backed form factor [18]. The most common microstrip antenna is the patch. This antenna typically operates by exciting the dominant TM_{10} cavity mode, which radiates broadside to the patch [19]. It is also possible to design a patch antenna to radiate parallel to the plane of the patch (i.e., at end-fire) by exciting the higher TM_{20} mode instead [19]. However, the footprint is larger; increased losses in higher-order modes can lead to lower efficiencies [20, 21]; and the feed network requires a special mechanism to avoid exciting lower modes in the patch cavity [22, 23]. Microstrip monopole antennas and planar inverted F-antennas (PIFAs) can also radiate at end-fire, but need to be arrayed to achieve bi-directional radiation patterns. Examples of these include a four-element uniplanar array with gain up to 8 dBi [24] and an arrangement of top-hat monopoles to form a Yagi-Uda antenna with uni-directional gain of 6.6 dBi [25]. Bi-directional patterns with moderate gains from 4.9 to 6.9 dBi have also been produced by shaping the field of a microstrip dipole antenna using high-impedance substrates [26, 27]; however, the polarization is parallel to the substrate and not suitable for mounting over a large ground plane.

Received 23 December 2021, Accepted 23 February 2022, Scheduled 8 March 2022

* Corresponding author: Masoud Ahmadi (masoud.ahmadi@ubc.ca).

[1] The University of British Columbia, Canada. [2] The Dominion Radio Astrophysical Observatory, Canada.

Over the last two decades, the development of electromagnetic metamaterials with exotic effective material parameters has led to improvements in the radiation performance of traditional antenna designs [28, 29]. In particular, due to their relatively simple fabrication process, single-negative metamaterials with either $\epsilon_r < 0$ or $\mu_r < 0$ have been popular for adoption in microstrip antenna design. For example, metamaterial loading has enabled antenna miniaturization [30], increased radiation efficiency [31], multi-band operation [32], and novel compact omnidirectional radiators based on zeroth-order resonances [33].

In this work, we use a negative permittivity substrate to realize a bi-directional radiation pattern with high directivity using a compact single-element microstrip patch antenna. We show that loading a narrow microstrip patch with a block of negative permittivity material produces a resonant mode with a nearly uniform electric field profile. This mode results in a high-gain end-fire antenna with a small footprint. The negative permittivity substrate acts as an effective inductor that resonates with the strong fringing capacitance formed between the patch and the ground. Nulls appear at broadside due to the field polarization as well as in the transverse plane due to the uniform patch fields, providing high directivity with good efficiency. A detailed theoretical model is presented and verified through full-wave simulation. A prototype is fabricated using a thin-wire medium to implement the negative permittivity substrate. The simulated response is then verified in the experiment at 10.8 GHz and shown to radiate with a bi-directional directivity of 10.7 dBi at 93% (simulated) efficiency and to operate over a 10-dB impedance bandwidth of 3.8%.

2. THEORETICAL ANTENNA DESIGN

2.1. Resonance Mechanism

In this section, we show that loading a patch antenna with a negative permittivity substrate can invoke a resonance between the fields under the patch and the fringing capacitance. Let us consider a rectangular microstrip patch of length l and width w placed over a dielectric substrate of thickness h and negative relative permittivity $\epsilon_r < 0$, as shown in Fig. 1(a). If the substrate is truncated, so it has the same lateral dimensions as the patch, we can model the capacitor of the patch as the parallel combination of two capacitors: a parallel-plate capacitance through the dielectric C_{pp} and a fringing capacitance through the surrounding air C_f. The negative permittivity modifies C_{pp} to produce a negative capacitance [34] that can be modeled as an effective inductance $L_{eff} = -1/\omega^2 C_{pp}$, as shown in Fig. 1(b).

The resonance between the fringing capacitance and the effective inductance occurs when the total capacitance of the patch $C_f + C_{pp}$ is equal to zero. We can estimate the value of the permittivity

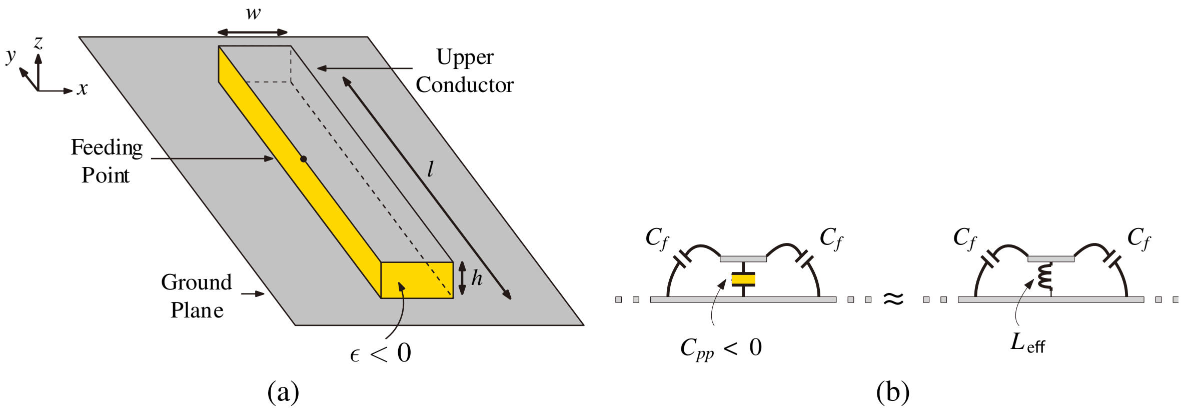

Figure 1. (a) The proposed patch antenna comprising a narrow strip loaded with a negative permittivity substrate. (b) The patch is modeled as a negative parallel-plate capacitance in parallel with the positive fringing capacitance. The negative capacitance acts like an effective inductance and resonates with the fringing capacitance.

required for resonance by approximating C_{pp} using the equations for idealized parallel-plate capacitance

$$C'_{pp} = -\frac{\epsilon_0|\epsilon_r|w}{h} = -|\epsilon_r|C'_{0,\,pp} \tag{1}$$

In these equations, primed variables represent per-unit-length parameters, while the subscript zero indicates capacitance with the dielectric removed. If we assume the fringing capacitance is weakly dependent on the permittivity of the truncated dielectric substrate, then we can approximate its value using

$$C'_f \approx C'_{0,\,f} = C'_{0,\,\mu s} - C'_{0,\,pp} \tag{2}$$

where $C'_{0,\,\mu s}$ is the total per-unit-length capacitance calculated using the well-known equations for the capacitance of a microstrip line [35]. The permittivity required for the patch to resonate is then determined through

$$\epsilon_r = -\frac{C'_f}{C'_{0,\,pp}} = -\left(\frac{C'_{0,\,\mu s}}{C'_{0,\,pp}} - 1\right). \tag{3}$$

Figure 2(a) displays the microstrip, parallel-plate, and fringing capacitances of the patch as a function of width-to-height ratio while Fig. 2(b) displays the corresponding relative permittivity required for resonance. A unity width-to-height ratio was chosen as a compromise between achieving a compact size and reducing the sensitivity to the antenna geometry. The sensitivity can be determined from the slope of the relative permittivity curve in Fig. 2(b). For example, narrower patches require larger negative permittivity values for resonance, and those larger values are more sensitive to changes in w/h. Furthermore, in anticipation of implementing the negative permittivity substrate using a thin-wire medium, the patch cannot be made too narrow; otherwise, the diameter of the wires in the thin-wire medium would have to be unrealistically small. Given the choice of $w/h = 1$, the corresponding relative permittivity can be determined from Fig. 2(b) to be $\epsilon_r = -2.0$. Note that these plots were generated from per-unit-length parameters, so the fringing capacitance at each end of the patch was not included in the analysis. By modeling the end capacitances using empirical equations for open microstrip stubs [36], the relative permittivity values required for resonance would be slightly more negative than those shown.

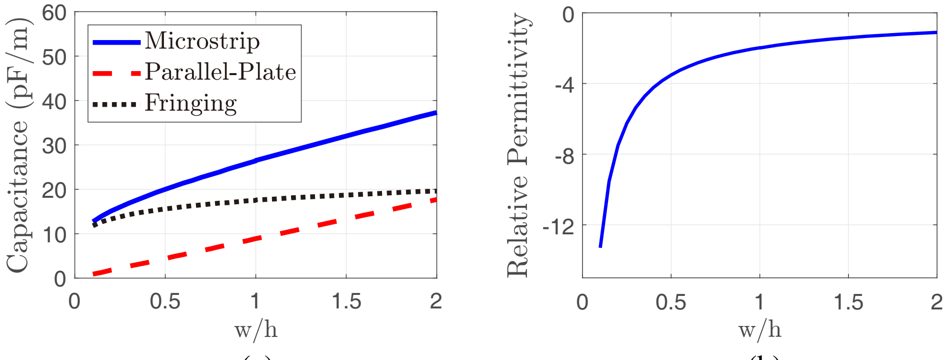

(a) (b)

Figure 2. (a) Per-unit-length patch capacitances as a function of patch geometry: free-space microstrip capacitance ($C'_{0,\,\mu s}$), free-space parallel-plate capacitance ($C'_{0,\,pp}$), and free-space fringing capacitance ($C'_{0,\,f}$). (b) The substrate relative permittivity required for resonance.

2.2. Electric Field Distribution

The microstrip patch was simulated using the full-wave finite-element solver in COMSOL Multiphysics [37] to verify the presence of a resonant mode. A narrow patch was considered, with a homogeneous, isotropic, and lossless dielectric truncated to the size of the patch. The patch was placed parallel to the xy plane with its width along the x axis and length along the y axis (as depicted in Fig. 1(a)). The ground plane was infinite, and all metal layers were perfectly conducting. By setting $w = h = 0.05\lambda$ and $l = \lambda$, where λ is the free-space wavelength, and exciting the patch at the midpoint of one of the long edges, a mode with quasi-uniform vertical electric fields (E_z) was observed over a range of dielectric constants from -2.4 to -3.5. Fig. 3 plots the fields excited over a patch with $l = \lambda$, $w = 0.05\lambda$, $h = 0.05\lambda$, and $\epsilon_r = -3$, where λ is the free-space wavelength. Here we can observe fields with a relatively uniform phase and amplitude across the length of the patch.

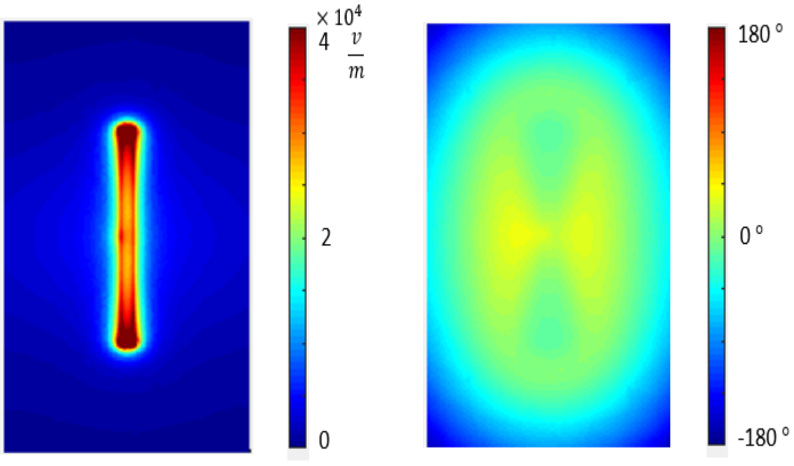

(a) (b)

Figure 3. (a) Magnitude and (b) phase of the electric field across a patch with a width of 0.05λ, a length of 1λ, a height of 0.05λ, and a substrate permittivity of -3. The substrate is truncated to the dimensions of the patch and placed on an infinite PEC ground plane. The electric field under the patch is aligned with the z axis and exhibits a uniform phase. These fields can be modeled as a uniform vertical displacement current density across the patch. (a) $|E_z|$, (b) $\angle E_z$.

The strong vertical fields produce a displacement current that provides the primary radiation mechanism of the antenna. These currents lead to a pattern null along z. By setting the patch length to λ, additional nulls are introduced along $\pm y$ to further increase the maximum directivity. More details will be provided on these nulls in the following section.

2.3. Calculated Radiation Pattern

The radiating patch can be modeled by a uniformly distributed vertical current density $\mathbf{J} = J_z\hat{\mathbf{z}}$. Since the width and height of the patch are electrically small, the current can be treated as a line distribution along the y axis without significantly affecting the resulting pattern. The currents are shown relative to the antenna geometry in Fig. 4(a). The current density can be described by the following expression

$$J_z(\mathbf{r}) = \begin{cases} J_0 hw\,\delta(x)\delta(z) & \text{if } |y| \le l/2 \\ 0 & \text{otherwise.} \end{cases} \tag{4}$$

The radiated field can be calculated by evaluating the radiation integral [19]

$$\mathbf{E}_{ff} = \hat{\boldsymbol{\theta}}\frac{jk\eta}{4\pi}\frac{e^{-jkr}}{r}\sin\theta \int J_z(\mathbf{r}')e^{jk\hat{\mathbf{r}}\cdot\mathbf{r}'}\,dv' \tag{5}$$

where k is the wave-number; η is the wave impedance; and the primed coordinates are used to integrate over the source currents. The spherical coordinates θ and ϕ are defined in Fig. 4(a). Since the currents are oriented parallel to the z axis, the electric far field will have only a θ component, and the field will be TM$_z$ polarized. The radiation intensity $U = |\mathbf{E}_{ff}|^2 r^2/2\eta$ can be calculated by evaluating Eq. (5) as

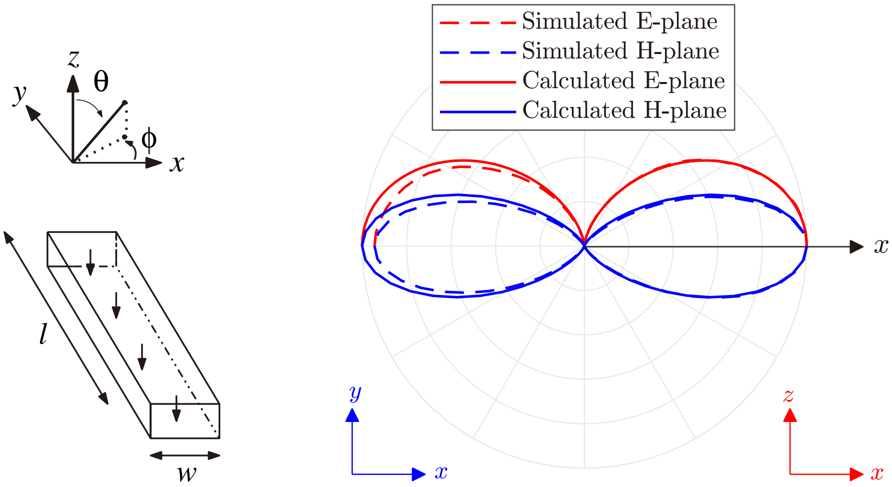

(a) (b)

Figure 4. (a) The patch is illustrated with the line distribution of vertical current elements used in the theoretical model. (b) The calculated and simulated normalized radiation intensity patterns are plotted along the E-plane (xz, red lines) and H-plane (xy, blue lines) in linear units. These patterns correspond to a patch of length λ, width 0.05λ, height 0.05λ, and substrate permittivity -3. The main lobes lie along $\pm x$ with a null at broadside and nulls along $\pm y$.

follows

$$\begin{aligned} U(\theta,\phi) &= \frac{k^2\eta}{32\pi^2}\left[hw\int_{-l/2}^{l/2} J_0 \sin\theta\, e^{jyk\sin\theta\sin\phi}\,dy\right]^2 && (6)\\ &= \frac{k^2\eta}{32\pi^2}h^2w^2J_0^2\sin^2\theta \mathrm{sinc}^2\left(\frac{kl}{2}\sin\theta\sin\phi\right), && (7)\end{aligned}$$

where $\mathrm{sinc}x$ is the unnormalized sinc function $\frac{\sin x}{x}$.

A patch length of $l = \lambda$ results in a normalized radiation pattern

$$\frac{U}{U_{\max}} = [\sin\theta\cdot\mathrm{sinc}(\pi\sin\theta\sin\phi)]^2 \tag{8}$$

This pattern has a null along the z axis (broadside to the patch) from the orientation of the radiating currents and nulls along the $\pm y$ axes (parallel to the long edge of the patch) from the length of the patch being equal to one wavelength. The direction of maximum radiation is along the $\pm x$ axes (parallel to the short edge of the patch).

In Fig. 4(b), we contrast the radiation pattern from Eq. (8) with the simulated far-field pattern corresponding to the field plots in Fig. 3 to show the accuracy of the model.

2.4. Input Impedance

In this section, we investigate the impact of patch length and substrate permittivity on input impedance. In order to efficiently match the antenna to a transmission-line feed, we require an input impedance that is close to $50\,\Omega$. Figs. 5(a) and 5(b) plot the input resistance and input reactance as a function of ϵ_r for several patch lengths l, as simulated in COMSOL Multiphysics. The patch width and substrate thickness are fixed at $w = 0.05\lambda$ and $h = 0.05\lambda$, respectively.

The directivity of the antenna is plotted in Fig. 5(c) to demonstrate the effect of changing substrate permittivity on radiation pattern. Since the antenna is designed to radiate bi-directionally along the x axis, the location of the feed point introduces an asymmetry in the physical structure (see Fig. 1(a)). We therefore define a bi-directional directivity D_{bd} as the *minimum* of the directivity along the $+x$

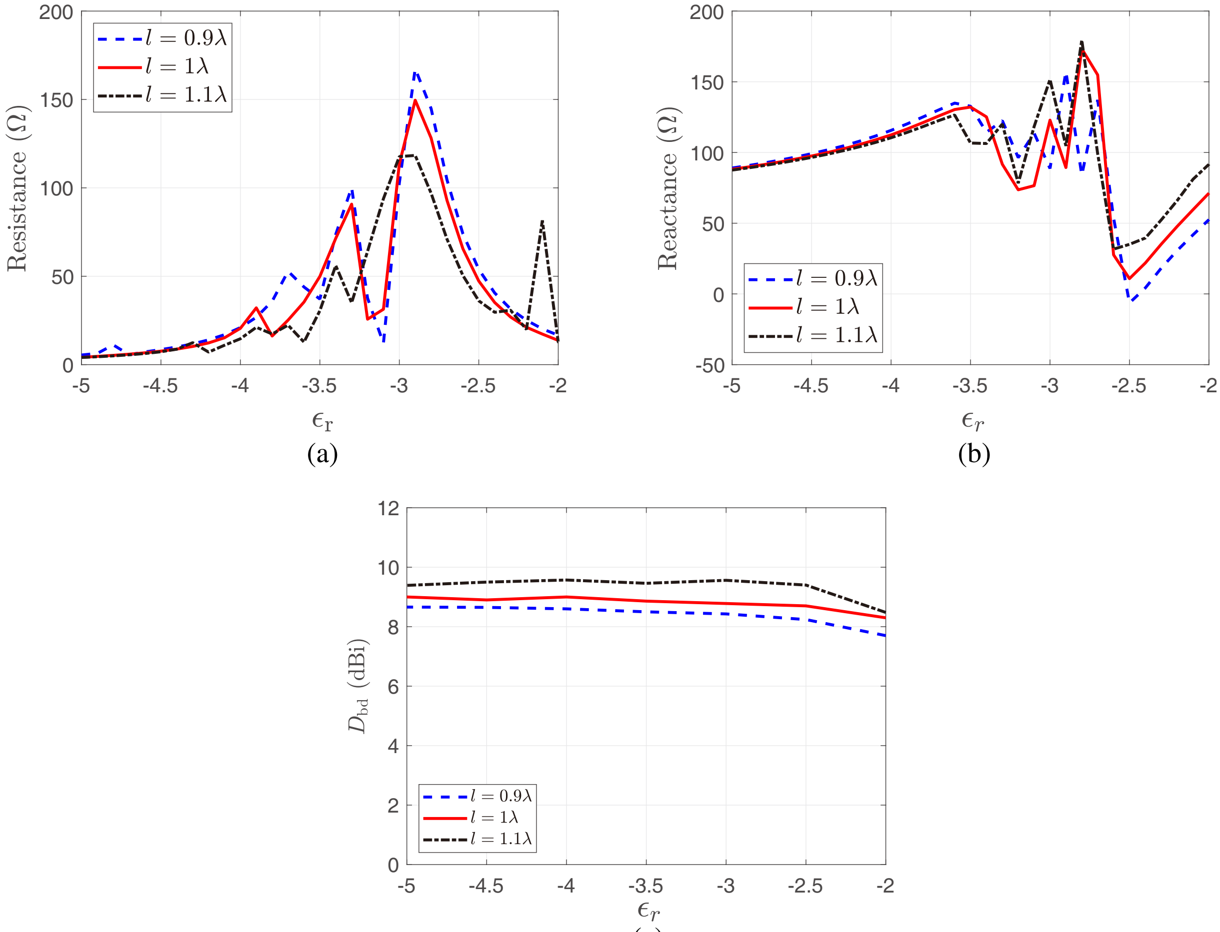

(a) (b)

(c)

Figure 5. The simulated (a) input resistance, (b) input reactance, and (c) bi-directional directivity $D_{bd} = \min(D_+, D_-)$ plotted against substrate permittivity for patch lengths of 0.9λ, 1λ, and 1.1λ. The substrate thickness and patch width are both fixed at 0.05λ.

direction, D_+, and the directivity along the $-x$ direction, D_-, to ensure that the directivity along one direction is not increased at the expense of the other.

The impedance undergoes a resonance between $-3.5 < \epsilon_r < -2.5$, with the reactance dropping near zero just above the resistance peak. Since the directivity is relatively stable over this region, we chose to operate with a relative permittivity -2.6 and patch length of 0.9λ in order to achieve the closest match to $50\,\Omega$. The current distribution across the patch is uniform here, with a bi-directional radiation pattern aligned with the x axis. The corresponding directivities are $D_+ = 8.4\,\mathrm{dBi}$ and $D_- = 8.2\,\mathrm{dBi}$, and the input impedance $58 + j6\,\Omega$.

3. PHYSICAL ANTENNA DESIGN

The antenna is designed to operate at X band and to be fabricated with a microstrip geometry. In order to realize a physical prototype, we will need to address three additional components. First, since materials with negative permittivity values close to zero do not exist at microwave frequencies, we need to produce a negative effective permittivity using a metamaterial substrate. Second, we need to address the finite extent of both the substrate and the ground plane. In simulation, the ground plane was infinite, and the substrate was truncated to the size of the patch. For compatibility with standard PCB fabrication technology, the ground plane and dielectric substrate should have the same finite footprint. Third, we need to design a matching network to match the antenna input impedance to $50\,\Omega$.

3.1. Negative Permittivity Substrate

In order to fabricate the end-fire patch antenna, we want the effective permittivity under the patch to be equal to $\epsilon_r = -2.6$. A thin-wire medium is well known to provide a negative permittivity Drude response with a plasma frequency determined by the wire geometry [38]. Given an array of z-directed wires of radius r suspended in a background medium of permittivity ϵ_m and arranged in a square lattice with spacing a, we have

$$\epsilon_{zz} = \epsilon_m \left(1 - \frac{\omega_p^2}{\omega^2}\right) \quad \text{where } \omega_p^2 = \frac{2\pi c^2}{a^2 \ln(a/r)}. \tag{9}$$

Here, ϵ_{zz} is the effective relative permittivity seen by z-polarized waves, and c is the speed of light in vacuum. The plasma frequency ω_p can be generalized to a rectangular array of spacing a_x and a_y using [39]

$$\omega_p^2 = \frac{\pi c^2}{a_x a_y} \frac{\ln(a_x/r) + \ln(a_y/r)}{\ln(a_x/r)\ln(a_y/r)}. \tag{10}$$

These equations are valid in the homogeneous limit for an infinite medium. In the case of a finite region with an electrically small transverse dimension, their accuracy decreases, and full-wave simulations must be used to account for fringing effects. We use them now to determine a starting via configuration to be used in simulation. Given the narrow geometry of the patch, we will implement the thin-wire medium using a linear array of vias. Ignoring fringing effects, we can therefore set $a_y = w$ and $a_x = l/N$, where N is the total number of vias.

The antenna is to be fabricated from Rogers Duroid 5880 laminate ($\epsilon_r = 2.2$ and $\tan\delta = 0.0009$). From Eq. (9), an effective permittivity of -2.6 at 10 GHz corresponds to a plasma frequency of 14.77 GHz. Given $w = 0.05\lambda = 1.5$ mm and $l = 0.9\lambda = 27.0$ mm, the via radius r was calculated using Eq. (10) for different N and tabulated in Table 1. As N increases, the corresponding radii decrease, presenting a tradeoff between ease of fabrication (thicker wires) and accuracy of the homogeneous approximation (more wires).

The minimum via radius available through our PCB fabrication process was $r = 0.2$ mm. According to Table 1, this radius corresponds to a solution between 3 and 4 vias distributed across the patch. These configurations are illustrated in Fig. 6(a) labeled as (i) and (ii), respectively. A third configuration is illustrated in Fig. 6(a) labeled as (iii), showing a four-via solution with via radii and spacing falling

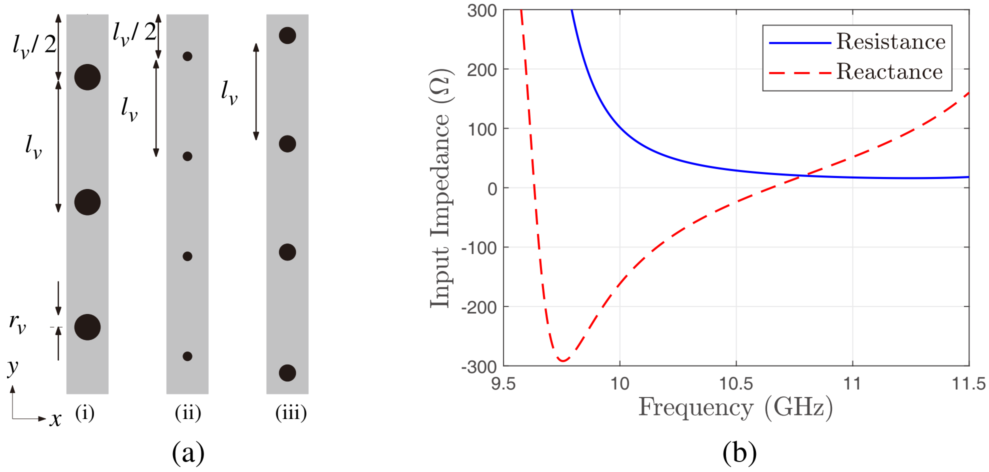

Figure 6. (a) The via configuration beneath the upper conductor to create a effective permittivity of -2.6. Case (i) considers 3 vias spaced by $l_v = 8.9$ mm, while cases (ii) and (iii) consider 4 vias spaced by $l_v = 6.7$ mm and $l_v = 8.7$ mm, respectively. (b) The input impedance of the patch antenna with via configuration given in case (iii). The patch is simulated with an infinite ground plane and infinite substrate layer.

Table 1. Number of vias, via radii, and via spacing corresponding to an effective medium with a relative permittivity of −2.6.

N	6	5	4	3	2
r_v (µm)	2.4	5.4	124	270	540
a_y (mm)	4.5	5.4	6.7	8.9	13.5

between those in (i) and (ii). This configuration was optimized through full-wave simulations in ANSYS HFSS to provide a resonance near 10 GHz while ensuring a bi-directional radiation pattern along x.

Figure 6(b) plots the input impedance of the antenna as a function of via radius given the four-via layout illustrated in configuration (iii) of Fig. 6(a). The antenna resonates at 10.8 GHz with an input impedance that is purely real and equal to 27 Ω. The simulated efficiency was over 90%.

3.2. Finite Ground Plane and Matching Network

In the previous section, simulations of the thin-wire medium were performed using laminates of infinite extent. The ground plane and substrate were both infinite, with the four vias providing an effective medium in the vicinity of the patch. Since the antenna radiates at end-fire, however, the radiated fields propagate along the laminate surface. Truncating the substrate and ground plane would therefore be expected to impact the antenna performance.

The effect of finite dimensions are characterized by simulating the radiation pattern as the size of the ground plane is varied. The input impedance was seen not to be significantly affected by the size of the ground plane. Consider a ground plane and substrate of length l_s and width w_s. The width is set to 44 mm to provide a ground for the fringing fields at either end of the patch. Because there are pattern nulls along y, increasing the width further has little effect on the radiation pattern. Conversely, changing the length has a pronounced effect on the radiation pattern. As l_s decreases, the main lobes of the antenna tilt upwards away from end-fire, and the bi-directional directivity decreases. The increased elevation angles are due to interference with radiating surface currents along the outside edges of the substrate and ground plane [40, 41]. Fig. 7 plots the elevation angle and bi-directional directivity of the antenna as a function of ground plane length, where the elevation angle is measured from the xy plane. From this figure, we choose a length of 3λ as a compromise between ground plane size and radiation performance. At this length, the elevation angle is 30°, and the bi-directional directivity is 10.1 dBi.

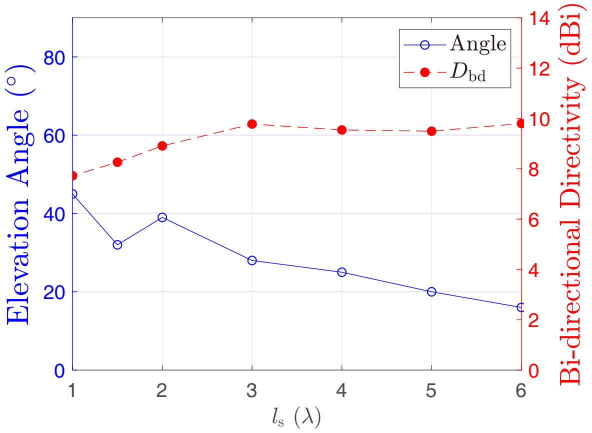

Figure 7. The elevation angle and bi-directional directivity of the antenna versus the ground plane length.

The finite ground plane antenna resonates with a resistance of approximately 35 Ω. A microstrip section of width 6.4 mm and length 4.9 mm provides a quarter-wavelength impedance match to the 50 Ω feed line. A short 1 mm section of transmission line acts as a buffer between the transformer and

Table 2. Dimensions of the final antenna layout depicted in Fig. 8(a).

Length	Value (mm)	Length	Value (mm)
w	1.5	w_1	4.8
l	28	w_2	6.4
l_1	34.5	h	1.57
l_2	4.9	l_v	8.7
l_3	1	r	0.26
w_s	44	l_s	86

the antenna patch to avoid detuning the antenna resonance frequency through interference with the fringing fields of the patch. The final antenna design is depicted in Fig. 8(a) with the corresponding parameters listed in Table 2. The surface current densities on the upper conductor and on the vias are depicted in Fig. 8(b). The horizontal surface currents are along the patch alternate directions and lead to radiation cancellation in the far-field. The vertical currents through the vias are all in phase and produce radiation in the direction parallel to the short sides of the patch (along the $\pm x$ axes). This is consistent with the vertical currents observed in Section 2.2 for the patch with a homogeneous negative permittivity substrate. The simulated radiation efficiency for this final design is 93%.

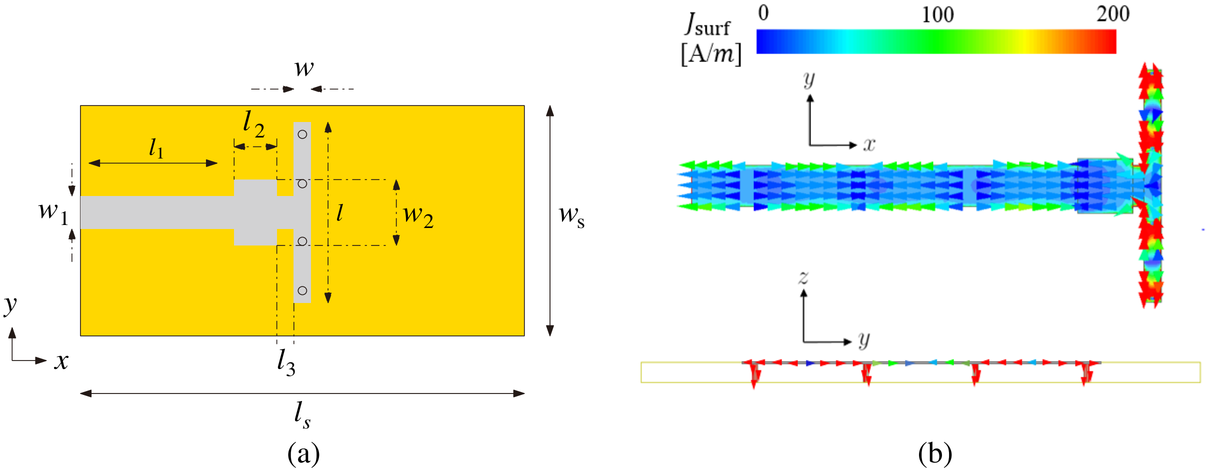

(a)

(b)

Figure 8. The final antenna design and layout is shown in (a). The surface currents are plotted in (b) over the upper conductor (viewed in the xy plane) and over the vias (viewed in the yz plane).

4. EXPERIMENTAL VERIFICATION

A prototype of the negative-permittivity patch antenna was fabricated by printing the pattern from Fig. 8(a) over a Rogers Duroid 5880 copper-clad laminate of thickness 1.57 mm. Four via holes were then drilled and plated between the patch and the ground plane. A photograph of the fabricated antenna is provided in Fig. 9(a).

The measured reflection coefficient, resistance, and reactance are displayed in Figs. 9(b)–9(d). Measurements were performed using a PNA-X vector analyzer from Keysight Technologies. The antenna resonates at 10.84 GHz with a resistance of 48 Ω and a 10-dB impedance bandwidth of 3.8%. This agrees closely with full-wave simulations of the final antenna design, which resonated at 10.8 GHz with resistance of 47 Ω and 10-dB impedance bandwidth of 3.4%.

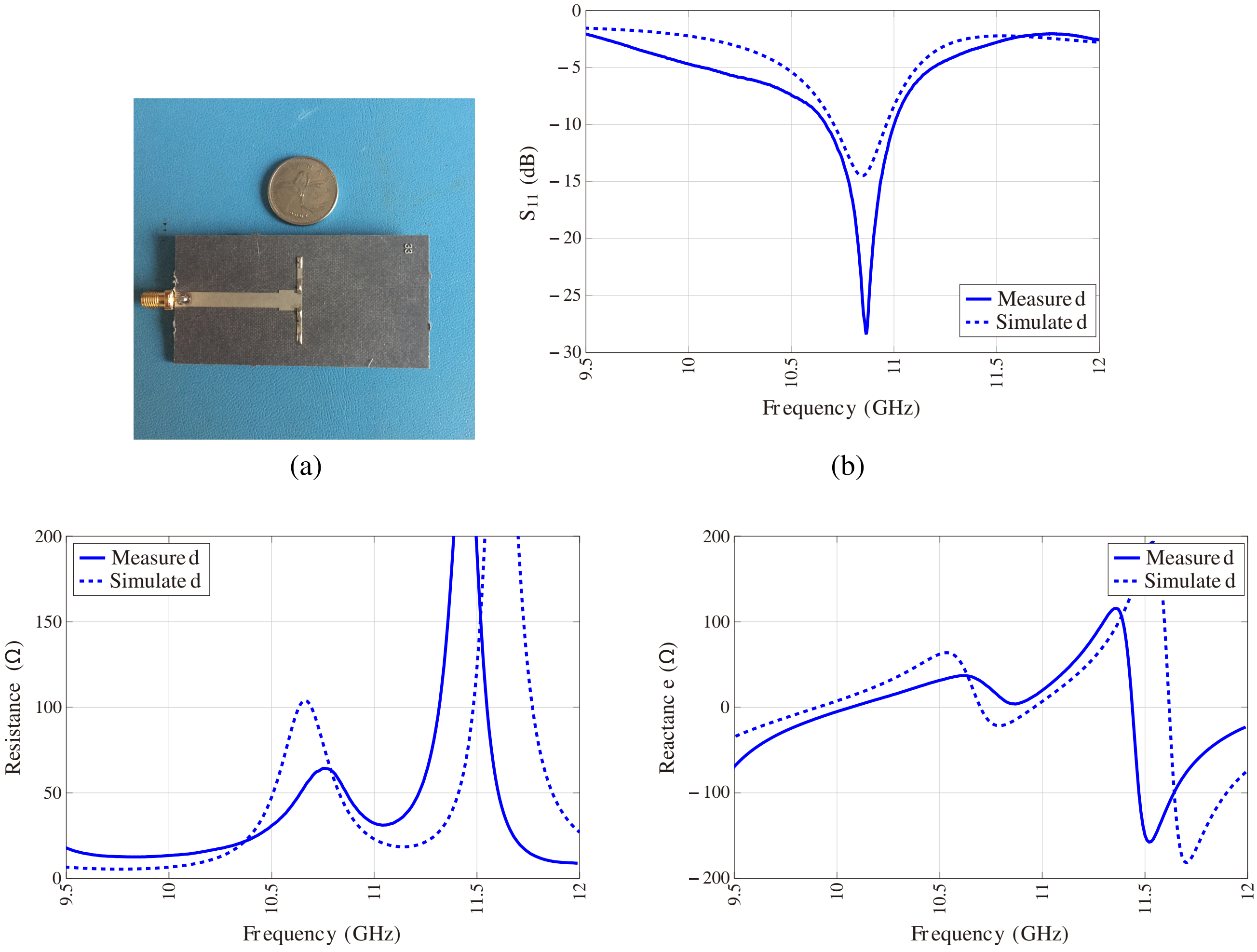

(a) (b)

(c) (d)

Figure 9. A photograph of the antenna prototype is depicted in (a). The antenna reflection coefficient and input impedance are plotted in (b) and (c).

Table 3. A comparison of our work to other planar bi-directional end-fire antennas in the literature. In the last two rows, the size column refers to the footprint of the top microstrip layer.

Reference	Element(s)	Feed(s)	Ground Plane	Size	D_{bd} (dBi)	Efficiency (%)	Frequency (GHz)
[1]	1	1	No	$0.53\lambda \times 0.47\lambda$	4.00	> 90	5.8
[9]	4	4	No	$1.40\lambda \times 0.60\lambda$	9.30	91	2.45
[10]	6	1	No	$2.70\lambda \times 0.28\lambda$	8.50	N/A	0.86
[11]	6	1	No	$2.40\lambda \times 0.13\lambda$	9.50	N/A	2.4
[12]	8	1	No	$3.34\lambda \times 0.72\lambda$	8.50	N/A	5.5
[17]	7	1	Yes	$1.30\lambda \times 0.60\lambda$	4.88	N/A	1.6
Our Work	1	1	Yes	$0.95\lambda \times 0.05\lambda$	10.70	> 90	10.8

Radiation patterns were measured using an Orbit/FR spherical near-field scanning system with a 959 Antenna Acquisition Module and SpectrumAnalysis near-to-far-field conversion software. Photographs of the experimental setup are shown in Figs. 10(a) and 10(b). The antenna was mounted

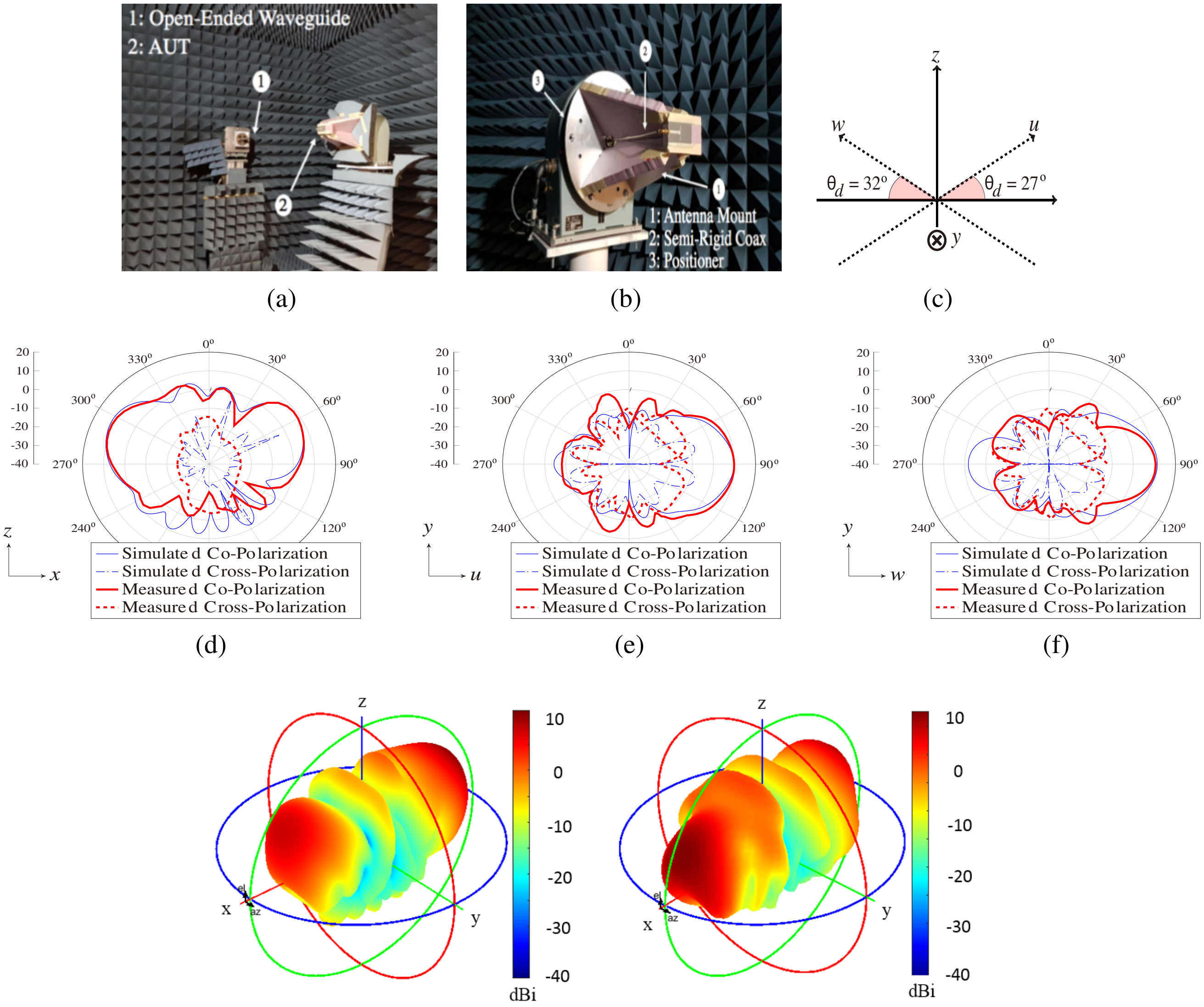

(a) (b) (c)

(d) (e) (f)

(g) (h)

Figure 10. The measured and simulated radiation patterns are plotted in dBi along the E and H planes. (a) A diagram of the main-beam axes used to define the H planes. (b) The E-plane (xz) radiation pattern. (c) The H-plane (uy) pattern at forward end-fire. (d) The H-plane (wy) pattern at backward end-fire. Simulated and measured 3D radiation patterns are depicted in (g) and (h), respectfully.

to a rotary positioner using a polystyrene foam support and connected to the RF port through a semi-rigid coaxial cable. An open-ended X-band rectangular waveguide sampled the fields.

Figure 10 displays the measured and simulated radiation patterns at 10.8 GHz for both co-polarized and cross-polarized fields. Since the main beams are tilted up from the xy plane, we define two new axes w and u to indicate the directions of maximum radiation, as illustrated in Fig. 10(c). The E plane corresponds to the xz plane and is plotted in Fig. 10(d). The H-plane fields are plotted separately for each beam, with Fig. 10(e) plotting the forward end-fire pattern over the uy plane and Fig. 10(f) plotting the backwards end-fire pattern over the wy plane. The 3D directivity patterns are plotted in Figs. 10(g) and 10(h). We can observe a slight front-to-back asymmetry in the field patterns due to the presence of the feed structure on one side of the patch. In experiment, the forward beam radiated at an elevation angle of 32° with a directivity of 10.7 dBi while the backwards beam radiated at an angle of

27° with a directivity of 11.7 dBi. The highest side lobe was -7.2 dB from the peak. The simulated and measured radiation patterns agree closely (the simulated bi-directional directivity was within 0.2 dB of the measured values while the side-lobe level was 0.3 dB lower than measured one), with slightly reduced back-radiation in the measured data most likely due to the presence of the metallic back-plate on the antenna positioner.

In Table 3, we compare this work with other published planar bi-directional end-fire antennas. The last two rows refer to microstrip antennas. We see from the bi-directional directivity and efficiency that this work provides the highest gain. Furthermore, the dimensions of the proposed antenna are smaller than every other antenna, except for the low-directivity loaded patch in [1].

5. CONCLUSION

In this paper, we present a low-profile compact microstrip patch antenna loaded with a negative permittivity substrate that radiates bi-directionally at end-fire. Four thin vias under the patch produce a negative effective capacitance which resonates with the fringing capacitance. The narrow patch width ensures strong fringing fields while the length is chosen to introduce transverse nulls. A large ground plane was added to minimize beam tilt, and a quarter-wavelength matching transformer was added to the feed. The antenna patch has a footprint of 28 mm × 1.5 mm and radiates at 10.8 GHz. The bidirectional directivity was measured to be 10.7 dBi, with a 10-dB impedance bandwidth of 3.8% and a simulated efficiency of 93%. The antenna is suitable for directive applications in low path loss environments in which the antenna needs to be mounted on ground planes or large conducting bodies, such as systems with radio-sensors and RFID tags, automotive and aviation systems, radar applications, and mine and tunnel communication links.

ACKNOWLEDGMENT

The authors acknowledge CMC Microsystems for the provision of CAD tools that facilitated this research. This work was supported by the Natural Sciences and Engineering Research Council of Canada (NSERC), the Canada Foundation for Innovation (CFI), the British Columbia Knowledge Development Fund (BCKDF), and the National Research Council (NRC).

REFERENCES

1. Ye, M., X. Li, and Q. Chu, "Single-layer single-fed endfire antenna with bidirectional circularly polarized radiation of the same sense," *IEEE Antennas and Wireless Propagation Letters*, Vol. 16, 621–624, 2017.
2. Arai, H. and K. Kohzu, "A bidirectional notch antenna," *IEEE Antennas and Propagation Society International Symposium, 1996 Digest*, Vol. 1, 42–45, Jul. 1996.
3. Rohani, B., K. Takahashi, H. Arai, Y. Kimura, and T. Ihara, "Improving channel capacity in indoor 4×4 MIMO base station utilizing small bidirectional antenna," *IEEE Transactions on Antennas and Propagation*, Vol. 66, No. 1, 393–400, 2018.
4. Zhao, Y., Z. Zhang, K. Wei, and Z. Feng, "A dual circularly polarized waveguide antenna with bidirectional radiations of the same sense," *IEEE Transactions on Antennas and Propagation*, Vol. 62, No. 1, 480–484, 2014.
5. Viezbicke, P. P., "Yagi antenna design," *Final Report National Bureau of Standards, Boulder, CO. Time and Frequency Div.*, 1976.
6. Jia, T. and X. Li, "A compact stacked bidirectional antenna for dual-polarized WLAN applications," *Progress In Electromagnetics Research C*, Vol. 44, 95–108, 2013.
7. Batgerel, A., J. I. Choi, and S. Y. Eom, "High-gain bidirectional MDAS antenna design excited by stacked-microstrip dipole," *Journal of Electromagnetic Waves and Applications*, Vol. 26, Nos. 11–12, 1412–1422, 2012.

8. Batgerel, A., S. Y. Eom, L. Minz, J. M. Kim, and J. I. Choi, “High gain bidirectional microstrip dipole antenna,” *2011 IEEE International Conference on Ultra-Wideband (ICUWB)*, 21–24, Sep. 2011.
9. Guo, H. and W. Geyi, “Design of bidirectional antenna array with adjustable endfire gains,” *IEEE Antennas and Wireless Propagation Letters*, Vol. 18, No. 8, 1656–1660, Aug. 2019.
10. Liu, L., Z. Zhang, Z. Tian, and Z. Feng, “A bidirectional endfire array with compact antenna elements for coal mine/tunnel communication,” *IEEE Antennas and Wireless Propagation Letters*, Vol. 11, 342–345, 2012.
11. Liu, W., Z. Zhang, Z. Tian, and Z. Feng, “A bidirectional high-gain cascaded ring antenna for communication in coal mine,” *IEEE Antennas and Wireless Propagation Letters*, Vol. 12, 761–764, 2013.
12. Tian, D., R. Xu, G. Peng, J. Li, Z. Xu, A. Zhang, and Y. Ren, “Low-profile high-efficiency bidirectional endfire antenna based on spoof surface plasmon polaritons,” *IEEE Antennas and Wireless Propagation Letters*, Vol. 17, No. 5, 837–840, 2018.
13. Liu, W., Y. Li, Z. Zhang, and Z. Feng, “A bidirectional array of the same left-handed circular polarization using a special substrate,” *IEEE Antennas and Wireless Propagation Letters*, Vol. 12, 1543–1546, 2013.
14. Cho, K. and T. Hori, “Bidirectional rod antenna composed of narrow patches,” *Proceedings of IEEE Antennas and Propagation Society International Symposium and URSI National Radio Science Meeting*, Vol. 1, 174–177, Jun. 1994.
15. Liu, F., Z. Zhang, W. Chen, Z. Feng, and M. F. Iskander, “An endfire beam-switchable antenna array used in vehicular environment,” *IEEE Antennas and Wireless Propagation Letters*, Vol. 9, 195–198, 2010.
16. Wang, R., B. Wang, G. Gao, X. Ding, and Z. Wang, “Low-profile pattern-reconfigurable vertically polarized endfire antenna with magnetic-current radiators,” *IEEE Antennas and Wireless Propagation Letters*, Vol. 17, No. 5, 829–832, May 2018.
17. Arai, H., K. Kohzu, T. Mukaiyama, and Y. Ebine, “Bi-directional notch antenna with parasitic elements for tunnel booster system,” *IEEE Antennas and Propagation Society International Symposium, 1997 Digest*, Vol. 4, 2218–2221, Jul. 1997.
18. Garg, R., P. Bhartia, I. J. Bahl, and A. Ittipiboon, *Microstrip Antenna Design Handbook*, Artech House, Boston, 2001.
19. Balanis, C. A., *Antenna Theory: Analysis and Design*, 4th Edition, John Wiley & Sons, New York, 2016.
20. Ahmadi, M., “Low-profile microstrip end-fire antennas based on metamaterial substrates,” Master’s thesis, University of British Columbia, 2018.
21. Bruneau, A., M. Bruneau, P. Herzog, and J. Kergomard, “Boundary layer attenuation of higher order modes in waveguides,” *Journal of Sound and Vibration*, Vol. 119, No. 1, 15–27, 1987.
22. Lin, Y.-D., J.-W. Sheen, and C.-K. Tzuang, “Analysis and design of feeding structures for microstrip leaky wave antenna,” *IEEE Transactions on Microwave Theory and Techniques*, Vol. 44, No. 9, 1540–1547, 1996.
23. Qian, Y., B. Chang, T. Itoh, K. Chen, and C. Tzuang, “High efficiency and broadband excitation of leaky mode in microstrip structures,” *1999 IEEE MTT-S International Microwave Symposium Digest*, Vol. 4, 1419–1422, IEEE, 1999.
24. Taheri, M. M. S., A. Abdipour, S. Zhang, and G. F. Pedersen, “Integrated millimeter-wave wideband end-fire 5G beam steerable array and low-frequency 4G LTE antenna in mobile terminals,” *IEEE Transactions on Vehicular Technology*, Vol. 68, No. 4, 4042–4046, 2019.
25. Hu, Z., Z. Shen, W. Wu, and J. Lu, “Low-profile top-hat monopole Yagi antenna for end-fire radiation,” *IEEE Transactions on Antennas and Propagation*, Vol. 63, No. 7, 2851–2857, Jul. 2015.
26. Li, M., S. Xiao, J. Xiong, and B. Wang, “Horizontal dipole located close to ground plane with bidirectional endfire radiation,” *IEEE Antennas and Wireless Propagation Letters*, Vol. 13, 1144–1147, 2014.

27. Li, M., Y. Zhang, and M. Tang, "Design of a compact, wideband, bidirectional antenna using index-gradient patches," *IEEE Antennas and Wireless Propagation Letters*, Vol. 17, No. 7, 1218–1222, Jul. 2018.
28. Nakano, H., *Low-Profile Natural and Metamaterial Antennas: Analysis Methods and Applications*, John Wiley & Sons, New York, 2016.
29. Eleftheriades, G. V. and N. Engheta, "Metamaterials: Fundamentals and applications in the microwave and optical regimes," *Proceedings of the IEEE*, Vol. 99, No. 10, 2011.
30. Bilotti, F., A. Alu, and L. Vegni, "Design of miniaturized metamaterial patch antennas with μ-negative loading," *IEEE Transactions on Antennas and Propagation*, Vol. 56, No. 6, 1640–1647, 2008.
31. Alù, A., F. Bilotti, N. Engheta, and L. Vegni, "Radiation properties of sub-wavelength resonant patch antennas filled with a pair of DPS, DNG, and/or SNG metamaterial blocks," *IEEE Antennas and Propagation Society International Symposium (APS/URSI)*, Washington, DC, 2005.
32. Alu, A., F. Bilotti, N. Engheta, and L. Vegni, "Subwavelength, compact, resonant patch antennas loaded with metamaterials," *IEEE Transactions on Antennas and Propagation*, Vol. 55, No. 1, 13–25, Jan. 2007.
33. Park, J.-H., Y.-H. Ryu, J.-G. Lee, and J.-H. Lee, "Epsilon negative zeroth-order resonator antenna," *IEEE Transactions on Antennas and Propagation*, Vol. 55, No. 12, 3710–3712, 2007.
34. Engheta, N. and R. W. Ziolkowski, *Metamaterials: Physics and Engineering Explorations*, John Wiley & Sons, New York, 2006.
35. Hammerstad, E. O., "Equations for microstrip circuit design," *5th European Microwave Conference, 1975*, 268–272, IEEE, 1975.
36. Edwards, T. C. and M. B. Steer, *Foundations for Microstrip Circuit Design*, 4th Edition, John Wiley & Sons, New York, 2016.
37. COMSOL Multiphysics v.5.5, www.comsol.com, COMSOL AB, Stockholm, Sweden, 2018.
38. Pendry, J. B., A. Holden, D. Robbins, and W. Stewart, "Low frequency plasmons in thin-wire structures," *Journal of Physics: Condensed Matter*, Vol. 10, No. 22, 4785, 1998.
39. Wu, Q., F.-Y. Meng, M.-F. Wu, J. Wu, and L.-W. Li, "Research on the negative permittivity effect of the thin wires array in left-handed material by transmission line theory," *Progress In Electromagnetics Research Symposium 2005*, 196–200, Hangzhou, China, Aug. 22–26, 2005.
40. Huang, J. and A. C. Densmore, "Microstrip Yagi array antenna for mobile satellite vehicle application," *IEEE Transactions on Antennas and Propagation*, Vol. 39, No. 7, 1024–1030, Jul. 1991.
41. Bhattacharyya, A. K., "Effects of finite ground plane on the radiation characteristics of a circular patch antenna," *IEEE Transactions on Antennas and Propagation*, Vol. 38, No. 2, 152–159, 1990.